IIETA International Information and Engineering Technology Association
Advancing the World of Information and Engineering

Journal Européen des Systèmes Automatisés
Vol. 59, No. 2, February, 2026, pp. 505-512
Journal homepage: http://iieta.org/journals/jesa

Effective Analysis of Permanent Magnet Positions on Electromagnetic Parameters of PMa-SynRMs

Hien Nguyen Thi Minh[1], Anh Quang Nguyen[2], Tu Pham Minh[2], Dinh Bui Minh[2], Chuong Trinh Trong[1], Vuong Dang Quoc[2*]

[1] School of Electrical and Electronic Engineering, Hanoi University of Industry, Ha Noi 100000, Vietnam
[2] School of Electrical and Electronic Engineering, Hanoi University of Science and Technology, Ha Noi 100000, Vietnam

Corresponding Author Email: vuong.dangquoc@hust.edu.vn

https://doi.org/10.18280/jesa.590219

Received: 14 December 2025
Revised: 10 February 2026
Accepted: 19 February 2026
Available online: 28 February 2026

Keywords:
PMa-SynRMs, permanent magnet position, electromagnetic torque, torque ripple, analytical model, finite element analysis

ABSTRACT

Electric permanent magnet assisted synchronous reluctance motors (PMa-SynRMs) merge the high saliency of synchronous reluctance motors (SynRMs) with supplementary torque from embedded permanent magnets (PMs), resulting in elevated torque per unit volume, improved power factor, and broader operational speed ranges. These attributes position PMa-SynRMs as ideal candidates for high-demand sectors like electric vehicle drives, industrial machinery, and renewable energy systems. This paper utilizes 2D finite element analysis (FEA) through Ansys Maxwell to examine how PM locations and sizes affect electromagnetic characteristics. A PMa-SynRM of 0.75 kW is designed. Three PM insertion points in the rotor barriers are assessed, along with sweeps of PM tangential width (0.5–1.0 per unit, pu) and radial thickness (1.0–1.5 pu). Focal metrics encompass torque magnitude, ripple ratio, flux density patterns, d-axis and q-axis inductances, flux linkages, power factor, and anti-demagnetization capability under d-axis current injection.

1. INTRODUCTION

In recent years, research on permanent magnet assisted synchronous reluctance motors (PMa-SynRMs) for applications in electric vehicles and industrial systems has increased significantly. Starting from simple initial approaches, magnets were introduced into the flux barriers. Various PMa-SynRM motor structures have been reported in the literature [1-3], and most PMa-SynRM designs generally follow the principle of circumferential rotor symmetry, which allows the definition of two symmetry axes, namely the d-axis and the q-axis. The results show that the magnet torque reaches its maximum value when the current vector is shifted by 90° relative to the magnet flux, while the reluctance torque reaches its maximum when the current vector lags behind the q-axis [4]. Since the addition of magnets in PMa-SynRM acts as flux assistance, it must be properly calculated and designed. The PMa-SynRMs have risen as leading choices for rigorous uses, including electrical vehicle (EV) traction needing strong launch torque and efficient cruising, plus compressors, blowers, and turbine drives in renewables [5]. The PMa-SynRM efficacy hinges on rotor layout, especially permanent magnet (PM) geometry in layered barriers. Faulty placement may cause flux imbalances, heightening ripple, demagnetization vulnerability during surges, and efficiency drops [6]. Dimensional factors like barrier-tangential width and radial depth influence linkage levels, risking bridge saturation or centrifugal strains compromising durability [7]. The PMa-SynRM research has matured, emphasizing rotor refinement to balance reluctance and alignment torques. Initial efforts clarified barrier functions in anisotropy creation and PM addition for torque uplift [8]. The finite element analysis (FEA) assessed layered barriers for broad constant-power and ripple lessening [9]. Volume reduction strategies proved 50% magnet savings viable with torque retention for extended speeds [10]. Recent explorations address fine PM geometry impacts. Asymmetric gap studies boosted density via position tweaks for ripple easing [11].

However, in current designs, an effective analysis of PM placement within the reluctance rotor has not been clearly discussed in previous studies, particularly with regard to magnet positioning. This evaluation aims to explore trends in investigating magnet placement at different design positions, assessing parameters such as flux linkage, inductance, torque, and power factor. Based on these analyses, conclusions can be drawn to determine the optimal magnet position and thereby enhance the overall performance of the electric machine.

In this research, the analytical model and FEA are presented to evaluate and analysise the performance of PMa-SynRMs taking the PM positions and size variations into account above problems. The obtained results will show the impacts on torque curves, inductance components (d- and q-axis), magnetic flux densities and back electromotive force (EMF). The proposed methods are validated on the practical PMa-SynRM.

2. ANALYTICAL BACKGROUND

One of the greatest challenges in SynRM design lies in the

complex rotor geometry. Essentially, the stator of a SynRM is identical to that of an induction motor of the same rating, but the rotor contains neither squirrel-cage bars nor field windings. Instead, multiple flux barriers are strategically created to maximize the inductance saliency ratio (Ld/Lq). Previous studies have indicated that there are two common geometric configurations of flux barriers, namely segmented flux barriers and concentrated flux barriers. The segmented flux barrier configuration is designed based on geometric parameters that are aligned to achieve an optimal saliency ratio (ξ = Ld/Lq). This type is widely used in the current manufacturing of synchronous reluctance motors due to its relatively simple punching die, high mechanical strength, and the ability to insert permanent magnets into the air gaps within the rotor. In contrast, the concentrated flux barrier configuration is constructed based on flux lines that are parallel to the magnetic flux paths, resulting in machines with very high saliency ratio. However, owing to its complex geometry, this type is only applied in applications requiring exceptionally high torque/power density.

To improve torque and power factor, permanent magnets are inserted into the rotor, transforming the machine into a PMa-SynRM. In Vietnam, industrial applications still predominantly rely on induction motors. As the country advances its industrialization and modernization, production lines are becoming increasingly sophisticated, demanding drive motors with higher efficiency, better controllability, and improved fault tolerance. Such motors must also deliver high torque density and a power factor that meets or exceeds the minimum requirements set by the national grid operator. The PMa-SynRM fully satisfies these requirements. Nevertheless, very few domestic publications address detailed design methodologies for either SynRM or PMa-SynRM. The PMa-SynRM rotor optimization entails balances in PM geometry for peak output with resource limits. Inner placements curb leakage but curb alignment torque; outer ones boost torque yet amplify demagnetization from fields [12]. Width tunes anisotropy (aim Ld/Lq >3), bounded by barriers; thickness elevates flux till saturation curbs efficiency [13]. Issues include: flux asymmetries yielding >5% ripple/noise; saturation capping heat; torque-demagnetization equilibrium in overloads; stresses from larger PMs at speed. This quantifies in a prototype for geometry guidance.

The vector equations of the SynRM in the *d*-, *q*- axis can be expressed as follows [14, 15]:

$$e_m = \frac{d\lambda_m}{dt} + j\omega\lambda_m \tag{1}$$

$$v = e_m + R_s i_s + j\omega L_{st} i_s \tag{2}$$

where,
- $v = v_d + j.v_q$ is the machine's terminal voltage vector;
- λ_m is the air gap linkage flux;
- L_{st} is the total winding leakage inductance;
- R_s is the winding resistance;
- $i_s = i_{sd} + ji_{sq}$ is the stator current vector;
- ω is the reference frame electrical angular speed;
- e_m is the air gap electromotive voltage.

In steady state, $\frac{d\lambda_m}{d_t} \approx 0$, the RMS value of E_m is determined as follows:

$$|E_m| = \sqrt{2} \cdot N_1 \cdot \pi L D f \hat{B}_{\delta 1} = \sqrt{2} \cdot \left(\frac{n_s q k_{w1}}{n_p}\right) \pi L D f \hat{B}_{\delta 1} \tag{3}$$

$$\arg(e_m) = \frac{\pi}{2} + \delta \tag{4}$$

where,
- n_s is the number of conductors per stator slot;
- q is the number of stator slot per pole per phase;
- C_s is the winding connection factor;
- L is the machine active length;
- D is the air gap diameter (mm);
- f is the supply frequency;
- N_1 is the winding equivalent number of turns per pole per phase;
- $\widehat{B_{\delta_1}}$ is the maximum amplitude of the air gap fundamental flux density (T).

The magnetizing current is defined [14-16]:

$$i_m = i_d + j.i_q \tag{5}$$

where, i_d is *d*-axis current (A) and i_q is the *q*-axis current (A).

The space vector of the back electromotive force is determined as [14]:

$$\begin{aligned} e_m &= j\omega\lambda_m j\omega\left(\lambda_{dm} + j\lambda_{qm}\right) \\ &= j.\omega.(L_{dm}(i_{dm}).i_{dm} \\ &\quad + j.L_{qm}.i_{qm} \end{aligned} \tag{6}$$

Flux linkage as a function of the magnetizing current [14]:

$$\lambda_m = L_m \cdot i_m \cong \begin{bmatrix} L_{dm}(i_{dm}) & \sim 0 \\ \sim 0 & L_{qm} \end{bmatrix} \cdot i_m \tag{7}$$

$$\begin{aligned} \lambda_m &= \lambda_{dm}(i_{dm}) + j \cdot \lambda_{qm}\left(i_{qm}\right) \\ &\cong \lambda_{dm}(i_{dm}) + j \cdot L_{qm} i_{qm} \end{aligned} \tag{8}$$

where, λ_{dm} and λ_{qm} are the flux linkages with *d*- and *q*- axis. The general expression can be defined as [15, 16]:

$$\lambda_{dm} = \lambda_{dm}\left(i_{dm}, i_{qm}, \vartheta\right) \tag{9}$$

$$\lambda_{qm} = \lambda_{qm}\left(i_{dm}, i_{qm}, \vartheta\right) \tag{10}$$

In *d*-*q* reference coordinate, one gets:

$$\lambda_d = L_d \cdot i_d, \qquad \lambda_q = L_q \cdot i_q \tag{11}$$

where, L_d is *d*-axis inductance (H) and L_q is *q*-axis inductance.

The power factor (PF) is given by [15-17]:

$$\begin{aligned} PF\& &= \cos\left(\tan^{-1}\left(\frac{\frac{L_{dm}}{L_{qm}}\frac{i_{dm}}{i_{qm}} + \frac{i_{qm}}{i_{dm}}}{\frac{L_{dm}}{L_{qm}} - 1}\right)\right) \\ &= (\xi - 1)\sqrt{\frac{\sin(2\theta)}{2(\tan\theta + \xi^2 \cot\theta)}} \end{aligned} \tag{12}$$

where, $\xi = \frac{L_{dm}(i_{dm})}{L_{qm}}$ is the saliency ratio. According to the study [18], one has: $\tan(\theta) = \sqrt{\xi}$. Thus, the PF is defined as:

$$PF|_{max} = \cos(\varphi_i)\,|_{max} = \frac{\xi - 1}{\xi + 1} \tag{13}$$

Electromagnetic torque of the PMa-SynRM is [19-22]:

$$T_{em-g} = \frac{3}{2}\frac{p}{2}\left(L_{dm}(i_{dm}) - L_{qm}\right) \cdot I_m^2 \sin(2\theta) \tag{14}$$

For a PMa-SynRM [17], one gets:

$$\lambda_d = L_d.i_d, \;\; \lambda_q = L_q.i_q - \lambda_m \tag{15}$$

The electromagnetic torque in Eq. (14) becomes:

$$T_{em-g} = \frac{3}{2}\frac{p}{2}\left(L_{dm}(i_{dm}) - L_{qm}\right) \cdot I_m^2 \sin(2\theta) + \frac{3}{2}\frac{p}{2}.\lambda_{mag}.\cos(\theta) \tag{16}$$

where, the term λ_{mag} is the magnetic flux of the PM.

3. APPLICATION TEST

Table 1. Input parameters of PMa-SynRM

Parameter	Value	Unit
Power	0.75	kW
Speed	1500	Rpm
Pole Number	4	pole
Terminal Voltage	400	V
Efficiency	82.5	%
Power Factor	0.72	

Table 2. Main dimensions of stator, rotor and permanent magnet (PM)

Parameter	Value	Unit
Inner stator diameter	76	mm
Outer stator diameter	125	mm
Stator length	70	mm
Slot number	36	track
Turn number per ended coil	85	Turn
Outer rotor diameter	75.5	mm
Shaft diameter	24	mm
Number of barriers	3	barrier
PM Type	NdFeB	
Remanent flux density	1.21	T
Magnetic coercive Field	-995	H
Length PM	8.8	mm
Width PM	3.0	mm
Width of barrier region (w_{ry1})	4.92	mm
Width of barrier region (w_{ry2})	4.89	mm
Width of barrier region (w_{ry3})	3.67	mm
Width of barrier region (w_{ry4})	2.97	mm

An application test is based the SynRM given in Table 1. The calculated results for the stator, rotor and PMs are described in Table 2.

Figure 1 illustrates the finite-element mesh of the motor, with a maximum element size of 2 mm in the iron core and 0.4 mm in the air-gap region to ensure computational accuracy.

The PM is considered with three positions as shown in Figure 2. The distribution of magnetic flux at PM position 1 (P1), PM position 2 (P2) and PM position 3 (P3) is pointed out in Figure 3, Figure 4 and Figure 5.

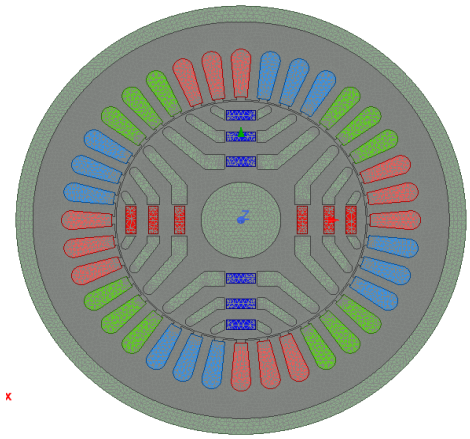

Figure 1. Finite element mesh of the proposed motor

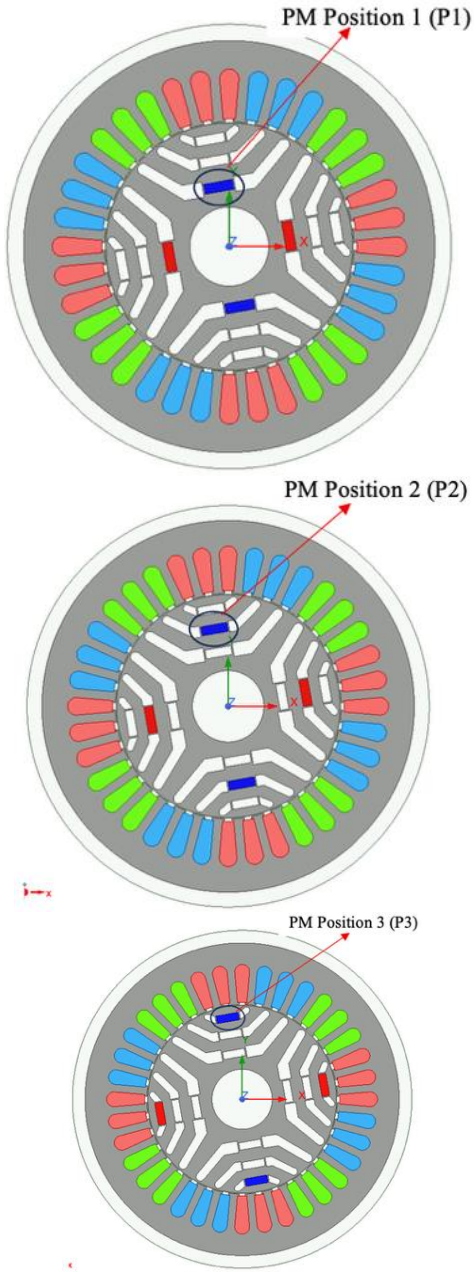

Figure 2. Modeling of PMa-SynRM with different permanent magnet (PM) positions

-At the PM position 1 (P1) (Figure 3): The magnetic flux lines are mainly concentrated in the iron bridges 1 and 2. This is the position where the flux generated by the permanent magnets almost entirely passes through the *d*-axis and the air gap, thereby minimizing leakage flux to the greatest extent possible. Under d-axis excitation, the magnetic flux density in the d-axis iron bridges reaches an average value of approximately 1.085 T. This region is also subjected to the most severe demagnetization effect. Accordingly, the magnet dimensions at this location can be optimized to ensure that the flux density in the steel barriers remains below the maximum allowable flux density on the rotor, thereby mitigating the risk of local magnetic saturation and demagnetization.

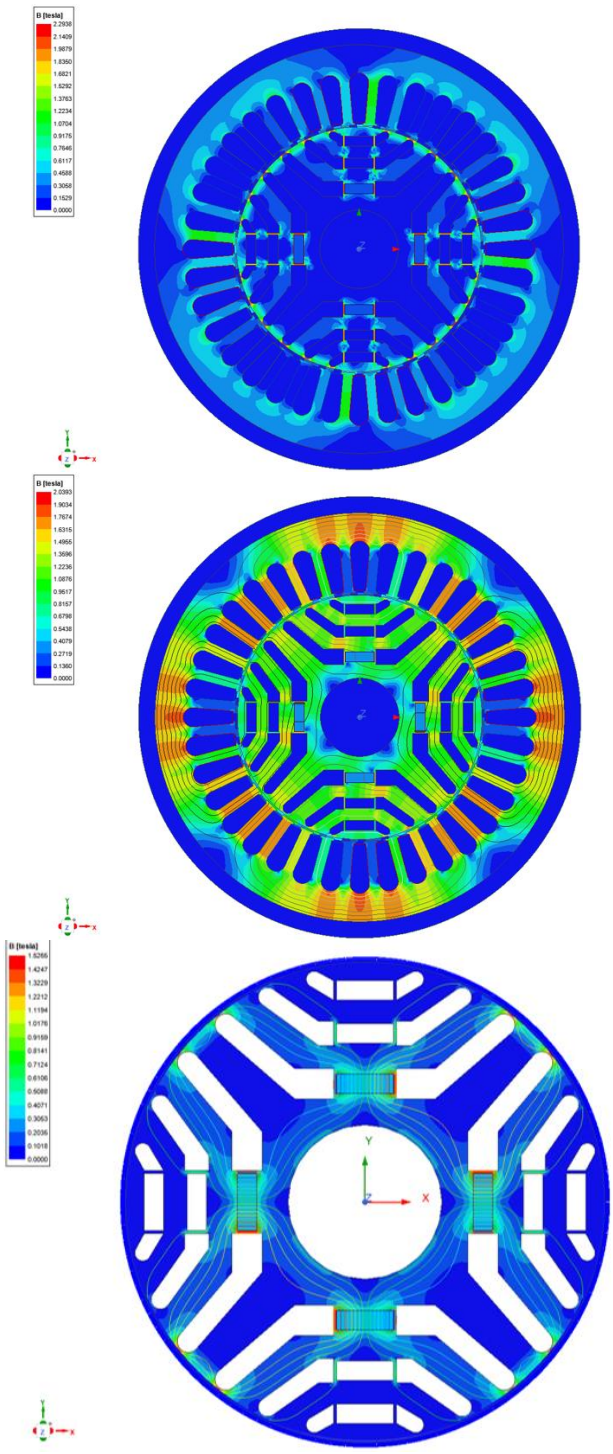

Figure 3. Distribution of magneic flux with three different PM positions: PM position 1

-At the PM position 2 (P2) (Figure 4): The magnetic flux lines, in the absence of excitation, are primarily distribute in the d-axis iron bridges 2 and 3. This is considered the position that directly contributes to the total torque of the machine due to the large iron flux path, which enhances the ability to control and guide the magnetic flux, while balancing L_d and L_q. Under d-axis excitation, the magnetic flux density at the d-axis iron bridges exhibits an average value of approximately 1.1 T. This region is subjected to a moderate level of demagnetization.

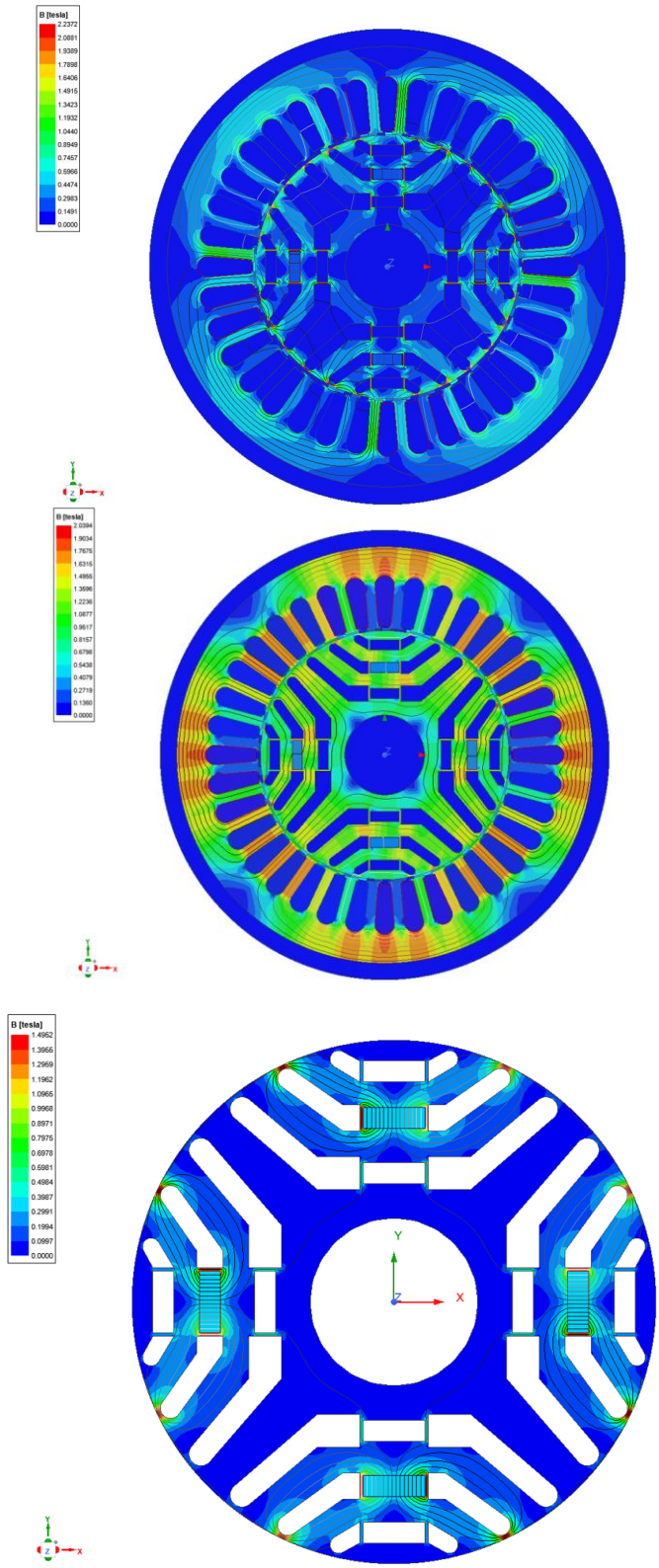

Figure 4. Distribution of magnetic flux with three different permanent magnet (PM) positions: PM position 2

-At the PM position 3 (P3) (Figure 5): The magnetic field lines when not stimulated are mainly distributed at slots 3, 4 of the iron core. These magnet positions are placed closest to the air gap, experiencing the most direct and intense impact from the reactive magnetic field. The magnetic flux density here can abruptly decrease under overload conditions, leading to the risk of local flux decrement, permanently weakening the magnetic flux. Under d-axis excitation, the magnetic flux density at the d-axis iron bridges reaches an average value of approximately 1.18 T. The edge and intermediate steel bridges between the flux-barrier regions are intentionally designed to operate in a saturated state during flux conduction, resulting in a sharp increase in their magnetic reluctance and consequently forcing the main magnetic flux to pass through the air gap.

Figure 6 illustrates the static electromagnetic torque of the PMa-SynRM for three different permanent magnet positions within the rotor. The results show that the maximum torque is obtained when the magnets are placed at Position 1, reaching approximately 4.38 Nm, followed by Position 2 (≈ 4.4 Nm) and Position 3 (≈ 5.44 Nm). This indicates that placing the magnets closer to the inner flux barriers (Position 1) enables more effective utilization of the permanent magnet flux in conjunction with reluctance torque. The improved torque performance at Position 1 can be attributed to reduced leakage flux and better alignment of the magnetic field along the d-axis, which enhances the combined reluctance and magnet torque components.

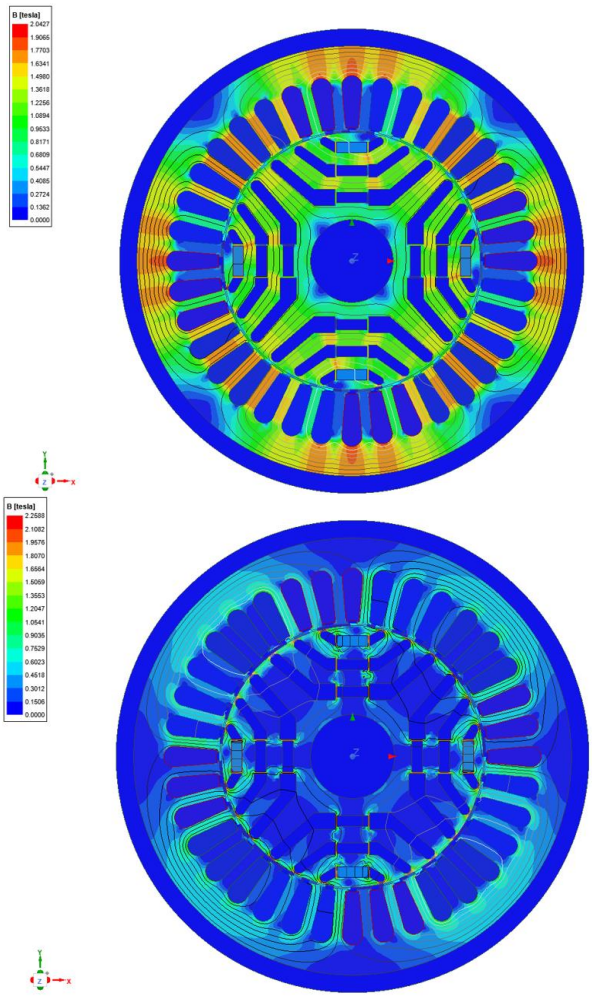

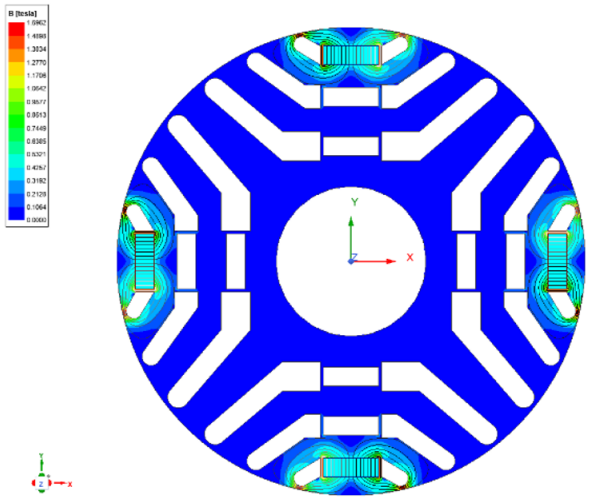

Figure 5. Distribution of magnetic flux with three different PM positions: PM position 3

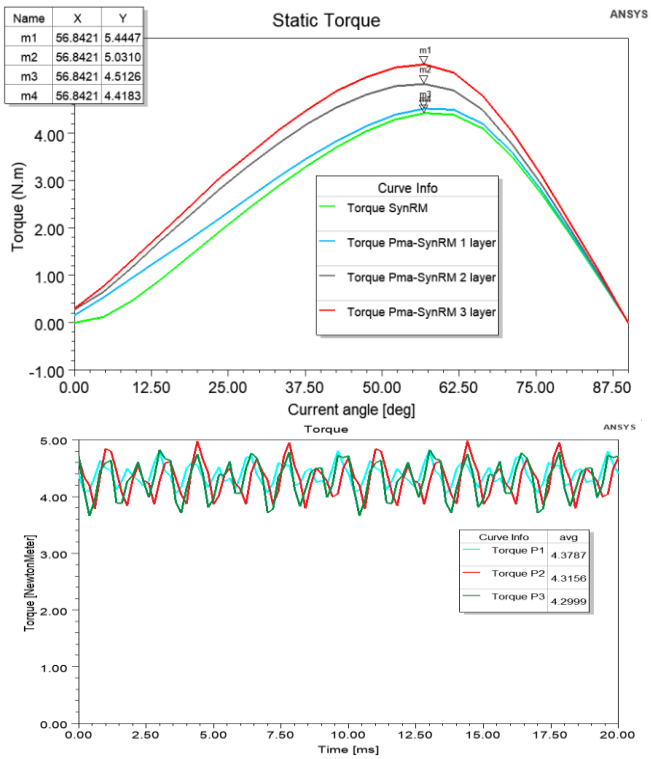

Figure 6. Comparision of torque waveform with different PM positions (1, 2 and 3)

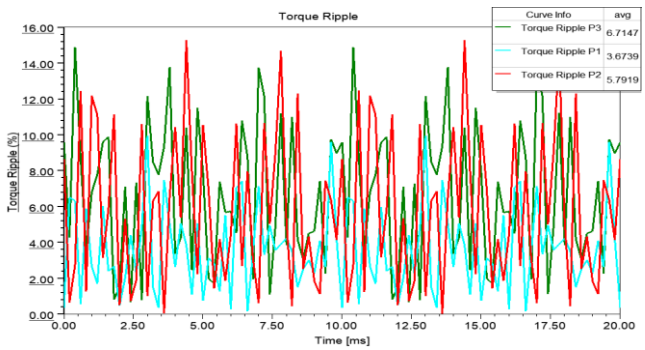

Figure 7. Torque ripple waveform of PMa-SynRM with different PM positions

Figure 7 compares the torque ripple corresponding to the three magnet positions. It is evident that Position 1 exhibits the lowest torque ripple, approximately 3.67%, whereas the ripple increases significantly at Position 3, reaching about 6.71%. The higher torque ripple at Position 3 is mainly caused by magnetic flux imbalance due to the magnets being located closer to the air gap, where they are more strongly affected by armature reaction and slotting effects. In contrast, Position 1 provides a more uniform air-gap flux distribution, which mitigates electromagnetic asymmetry and reduces torque pulsations.

Figure 8 presents the time-domain variation of the d-axis and q-axis inductances for the PMa-SynRM with three different permanent magnet positions (P1, P2, and P3). Overall, the inductance waveforms exhibit small periodic ripples superimposed on nearly constant average values, indicating stable magnetic behavior with limited saturation effects. For the d-axis inductance (L_d), the average values are relatively close across all magnet positions, with approximately 0.5735 H (P1), 0.5696 H (P2), and 0.5760 H (P3). This confirms that the magnet position has a negligible influence on the d-axis inductance, as the *d*-axis magnetic circuit is primarily governed by the rotor iron geometry rather than the magnet placement. The small oscillations observed in L_d are mainly caused by slotting effects and rotor position-dependent permeance variations. In contrast, the q-axis inductance (L_q) shows a clearer dependence on magnet position. The average L_q increases from 0.1765 H (P1) to 0.1787 H (P2) and reaches the highest value of 0.1869 H (P3). This trend indicates that placing the magnets closer to the air gap (as in Position 3) reduces the magnetic reluctance along the q-axis, thereby increasing L_q. However, this also reduces the saliency ratio L_d/L_q, which can negatively affect torque production and power factor.

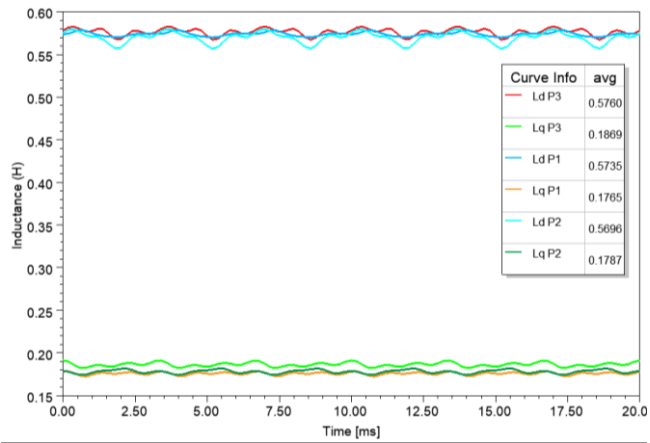

Figure 8. Inductances of PMa-SynRM with different PM positions

Figure 9 illustrates the relationship between flux linkage and stator current for the PMa-SynRM at different permanent magnet positions (P1, P2, and P3) under two current angle conditions, namely 0° and 90°. The curves provide insight into how magnet placement influences the magnetic behavior along the d- and q-axes. When the current angle is 0°, the flux linkage increases almost linearly with stator current at low current levels and gradually saturates as the current approaches higher values. The nearly overlapping curves for P1, P2, and P3 indicate that the d-axis flux linkage is largely independent of magnet position. This behavior confirms that the d-axis magnetic circuit is primarily dominated by the rotor iron geometry rather than the permanent magnet placement. The slight nonlinearity observed at higher currents is attributed to magnetic saturation in the rotor core. In contrast, when the current angle is 90°, the flux linkage remains close to zero across the entire current range for all magnet positions. This indicates that the q-axis flux linkage contributed by the permanent magnets is negligible, and the q-axis magnetic path is dominated by reluctance effects. The nearly flat curves further demonstrate that changes in magnet position have minimal impact on q-axis flux linkage under this excitation condition.

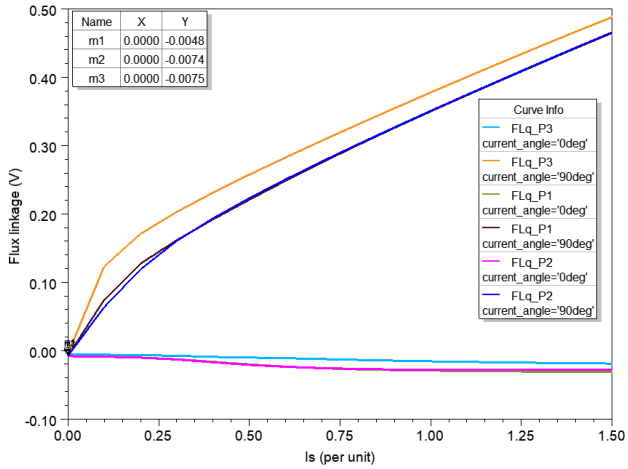

Figure 9. Flux linkage of PMa-SynRM with different PM positions

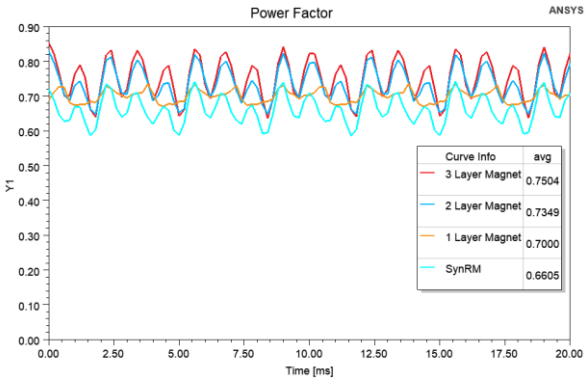

Figure 10. Power factor of PMa-SynRM with different PM positions

Figure 10 points out the power factor waveform of PMa-SynRM with different PM positions. The results show that the number of magnet layers on the rotor directly affects the power factor. Increasing the number of magnets enhances the magnetic flux linkage λ_m, which reduces the q-axis inductance and consequently improves the power factor $(\cos \varphi = L_d/L_q)$. However, the flux density distributions for one-, two-, and three-layer magnet configurations indicate that additional magnet layers increase the flux density in the rotor iron regions. Among them, Position 1 (P1) achieves the highest average power factor (~0.70), attributed to a higher saliency ratio and a more favorable balance between d- and q-axis inductances, resulting in reduced reactive power. Position 2 (P2) presents a slightly lower average value (~0.695) with larger oscillations, indicating moderate degradation in flux–current alignment. Position 3 (P3) shows the lowest average

power factor (~0.682) and the largest fluctuations, mainly due to increased q-axis inductance, reduced saliency ratio, and stronger armature reaction effects caused by magnets being closer to the air gap.

4. CONCLUSIONS

Through the analysis process, the results demonstrate that position 1 produces the lowest flux density on the steel regions, however the torque output is the highest, so the priority for embedding PM is Position 1 to save the amount of PM used. The flux linkage and d-axis inductance are independent of the location and quantity of PM. The power factor of the motor is affected by the location and quantity of PM. Therefore, a multi-layer design will improve the power factor but careful consideration of the structural strength is required. Increasing the magnet width can improve the torque, but is limited by the calculated size of the magnetic flux barriers. Increasing the magnet thickness can improve the torque, but is limited by the saturation on the steel regions of the rotor and the mechanical strength of the rotor. Increasing the magnet thickness gives a larger Lq drop, thereby improving the torque and power factor. The magnet size area at position 1 is the widest, which can effectively improve the torque and avoid centrifugal force and demagnetization, so it is preferred to add auxiliary magnets. These findings provide an important theoretical foundation that will enable domestic researchers and engineers to achieve faster and more effective design outcomes when developing a synchronous motor.

ACKNOWLEDGEMENTS

This research is funded by Hanoi University of Industry under project number 10-2024-RD/HD-ĐHCN.

REFERENCES

[1] Zhao, W., Xing, F., Wang, X., Lipo, T.A., Kwon, B.I. (2017). Design and analysis of a novel PM-assisted synchronous reluctance machine with axially integrated magnets by the finite-element method. IEEE Transactions on Magnetics, 53(6): 1-4. https://doi.org/10.1109/TMAG.2017.2662717

[2] Cai, H., Guan, B., Xu, L. (2014). Low-cost ferrite PM-assisted synchronous reluctance machine for electric vehicles. IEEE Transactions on Industrial Electronics, 61(10): 5741-5748. https://doi.org/10.1109/TIE.2014.2304702

[3] Bianchi, N., Fornasiero, E., Ferrari, M., Castiello, M. (2015). Experimental comparison of PM-assisted synchronous reluctance motors. IEEE Transactions on Industry Applications, 52(1): 163-171. https://doi.org/10.1109/TIA.2015.2466623

[4] Mohammadi, A., Mirimani, S.M. (2020). Design and analysis of a novel permanent magnet assisted synchronous reluctance machine using finite-element-method. In 2020 11th Power Electronics, Drive Systems, and Technologies Conference (PEDSTC), Tehran, Iran, pp. 1-5. https://doi.org/10.1109/PEDSTC49159.2020.9088379

[5] Kim, W.H., Kim, K.S., Kim, S.J., Kang, D.W., Go, S.C., Chun, Y.D., Lee, J. (2009). Optimal PM design of PMA-SynRM for wide constant-power operation and torque ripple reduction. IEEE Transactions on Magnetics, 45(10): 4660-4663. https://doi.org/10.1109/TMAG.2009.2021847

[6] Bianchi, N. (2013). Synchronous reluctance and interior permanent magnet motors. In 2013 IEEE Workshop on Electrical Machines Design, Control and Diagnosis (WEMDCD), Paris, France, pp. 75-84. https://doi.org/10.1109/WEMDCD.2013.6525167

[7] Guglielmi, P., Boazzo, B., Armando, E., Pellegrino, G., Vagati, A. (2012). Permanent-magnet minimization in PM-assisted synchronous reluctance motors for wide speed range. IEEE Transactions on Industry Applications, 49(1): 31-41. https://doi.org/10.1109/TIA.2012.2229372

[8] Montalvo-Ortiz, E.E., Foster, S.N., Cintron-Rivera, J.G., Strangas, E.G. (2013). Comparison between a spoke-type PMSM and a PMASynRM using ferrite magnets. In 2013 International Electric Machines & Drives Conference, Chicago, IL, USA, pp. 1080-1087. https://doi.org/10.1109/IEMDC.2013.6556230

[9] Diao, C., Zhao, W., Liu, Y., Wang, X. (2023). Permanent magnet assisted synchronous reluctance motor with asymmetric rotor for high torque performance. CES Transactions on Electrical Machines and Systems, 7(2): 179-186. https://doi.org/10.30941/CESTEMS.2023.00016

[10] Sultan, A.J., Abdollahi, S.E., Gholamian, S.A. (2026). Design optimization of a permanent magnet-assisted synchronous reluctance motor. International Journal of Engineering, 39(3): 658-667. https://doi.org/10.5829/ije.2026.39.03c.08

[11] Mousavi Bafrouei, S.M., Aliabad, A.D., Amiri, E. (2024). Design and analysis of PM-assisted synchronous reluctance machine with shifted magnetic poles. IET Electric Power Applications, 18(1): 52-63. https://doi.org/10.1049/elp2.12366

[12] Moghaddam, R.R., Gyllensten, F. (2013). Novel high-performance SynRM design method: An easy approach for a complicated rotor topology. IEEE Transactions on Industrial Electronics, 61(9): 5058-5065. https://doi.org/10.1109/TIE.2013.2271601

[13] Pellegrino, G., Vagati, A., Guglielmi, P., Boazzo, B. (2011). Performance comparison between surface-mounted and interior PM motor drives for electric vehicle application. IEEE Transactions on Industrial Electronics, 59(2): 803-811. https://doi.org/10.1109/TIE.2011.2151825

[14] Haataja, J. (2003). A comparative performance study of four-pole induction motors and synchronous reluctance motors in variable speed drives. Lappeenranta University of Technology, Lappeenranta, Finland.

[15] Kazakbaev, V.M., Prakht, V.A., Dmitrievskii, V.A. (2017). A comparative performance analysis of induction and synchronous reluctant motors in an adjustable-speed electric drive. Russian Electrical Engineering, 88(4): 233-238. https://doi.org/10.3103/S1068371217040095

[16] Moghaddam, R.R., Magnussen, F., Sadarangani, C., Lendenmann, H. (2008). New theoretical approach to the synchronous reluctance machine behavior and performance. In 2008 18th International Conference on Electrical Machines, Vilamoura, Portugal, pp. 1-6. https://doi.org/10.1109/ICELMACH.2008.4799845

[17] Jamali Fard, A., Mirsalim, M. (2022). Proposing a

sequential iterative method based on a per-unit model for rotor shape optimization in permanent magnet assisted synchronous reluctance motors. COMPEL-The International Journal for Computation and Mathematics in Electrical and Electronic Engineering, 41(5): 1826-1848. https://doi.org/10.1108/COMPEL-09-2021-0340

[18] Cong, T.T., Canova, A., Minh, D.B., Doan, B.T., Quoc, V.D. (2025). Optimal design of six-phase outer-rotor permanent magnet synchronous motor via the particle swarm technique. In 2025 25th International Conference on the Computation of Electromagnetic Fields (COMPUMAG), Naples, Italy, pp. 1-6. https://doi.org/10.1109/COMPUMAG60611.2025.11421278

[19] Do Chi, P., Hoang, B.H., Vuong, D.Q., Dinh, B.M. (2025). Analytical and finite element methods for evaluative electromagnetic parameters of inset PMSM and SPMSM. Journal Européen des Systèmes Automatisés, 58(2): 337-343. https://doi.org/337.10.18280/jesa.580214

[20] Cong, T.T., Thanh, B.D., Minh, D.B., Thao, N.G.M., Quoc, V.D. (2025). A Combinatory Analytical and Finite Element Approach for Comparing Electromagnetic Performance in IPM and SPM Synchronous Motors. Journal of Electromagnetic Engineering and Science, 25(4): 361-370. https://doi.org/10.26866/jees.2025.4.r.307

[21] Bianchi, N., Mahmoud, H., Bolognani, S. (2016). Fast synthesis of permanent magnet assisted synchronous reluctance motors. IET Electric Power Applications, 10(5): 312-318. https://doi.org/10.1049/iet-epa.2015.0240

[22] Huynh, T.A., Hsieh, M.F., Shih, K.J., Kuo, H.F. (2017). Design and analysis of permanent-magnet assisted synchronous reluctance motor. In 2017 20th International Conference on Electrical Machines and Systems (ICEMS), pp. 1-6. https://doi.org/10.1109/ICEMS.2017.8056462